applied sciences

MDPI

Article

Investigation of Flow Characteristics in Valveless Piezoelectric Pumps with Airfoil Baffles at Varying Angles of Attack

Jun Huang [1], Hiba Affane [1], Bo Zhang [2,*], Ming Kuang [1], Jian Xiong [1] and Siyao Zhang [3]

[1] Research Center of Fluid Machinery Engineering and Technology, Jiangsu University, Zhenjiang 212013, China; huangjun@ujs.edu.cn (J.H.); 5102210316@stmail.ujs.edu.cn (H.A.); 2222211057@stmail.ujs.edu.cn (M.K.); 2222211017@stmail.ujs.edu.cn (J.X.)
[2] College of Energy and Power Engineering, Nanjing University of Aeronautics and Astronautics, Nanjing 210016, China
[3] School of Mechanical Engineering, Jiangsu University, Zhenjiang 212013, China; 3220301200@stmail.ujs.edu.cn
* Correspondence: zhangbo_pe@nuaa.edu.cn

Abstract: To investigate the impact of airfoil angle of attack on the output performance of a valveless piezoelectric pump with airfoil baffles, this study conducted comprehensive performance tests and full-flow field simulations of piezoelectric pumps across a range of angles. At a driving voltage of 100 V and with a Clark Y airfoil set at an angle of 0°, the piezoelectric pump reached a peak output flow rate of 200.7 mL/min. An increase in the angle of attack corresponded to a decline in both the maximum output flow rate and the maximum back pressure of the pump. Flow field simulation results demonstrated that an increased airfoil angle of attack led to a gradual increase in entropy production within the piezoelectric pump. Turbulent dissipation and wall entropy production were found to be more pronounced compared to viscous entropy production. High turbulent dissipation was primarily observed at the pump chamber inlet, the trailing edges of the airfoils in both the inlet and outlet pipes, and the outlet bend. As the angle of attack increased, the complexity of the vortex core structures within the flow field escalated as well. Regions with significant wall entropy production were notably concentrated at the outlet bend.

Keywords: piezoelectric actuator; micropump; airfoil; vortex; entropy generation

check for updates

Academic Editor: Guillermo Hauke

Received: 31 October 2024
Revised: 27 December 2024
Accepted: 2 January 2025
Published: 6 January 2025

Citation: Huang, J.; Affane, H.; Zhang, B.; Kuang, M.; Xiong, J.; Zhang, S. Investigation of Flow Characteristics in Valveless Piezoelectric Pumps with Airfoil Baffles at Varying Angles of Attack. *Appl. Sci.* **2025**, *15*, 445. https://doi.org/10.3390/app15010445

Copyright: © 2025 by the authors. Licensee MDPI, Basel, Switzerland. This article is an open access article distributed under the terms and conditions of the Creative Commons Attribution (CC BY) license (https://creativecommons.org/licenses/by/4.0/).

1. Introduction

Piezoelectric micropumps, driven by piezoelectric actuators, are characterized by high energy density, rapid response, absence of electromagnetic interference, and low energy consumption [1–3]. These attributes render them highly suitable for a broad range of applications in fields like biomedical engineering [4,5], thermal management [6], microfluidic systems [7], and fuel cells [8]. Among the varieties of piezoelectric pumps, valveless piezoelectric pumps are favored by researchers due to their simple structure and lack of internal moving valves, which facilitate processing and miniaturization [9,10]. However, the structural characteristics of valveless piezoelectric pumps also lead to issues such as high output backflow and inferior performance.

To enhance the output performance of valveless piezoelectric pumps, extensive research has been conducted by scholars focusing on structural design, primarily involving the development of channels with differential flow resistance. Currently, channels with differential flow resistance commonly utilized in valveless piezoelectric pumps include diffusion tubes [11], Tesla tubes [12], Y-shaped tubes [13], vortex tubes [14], and heart-shaped tubes [15]. These channels exhibit resistance differences during the forward and

reverse flow of fluids, thereby possessing unidirectional shut-off capabilities that can substitute for moving valves within valveless pumps. Zhang et al. [16] discovered that placing structurally asymmetric baffles within the pump chamber can also configure a valveless piezoelectric pump. Consequently, various types of baffles, such as conical [17], trapezoidal [18], hemispherical [19], and triangular [20] baffles, have been implemented in valveless piezoelectric pumps. In our team's previous research, an airfoil structure was introduced into a piezoelectric pump, resulting in the design of a high-flow valveless piezoelectric pump with airfoil baffles [21]. Experimental results indicated that with a driving voltage of 100 V, the maximum output flow rate of the valveless piezoelectric pump with airfoil baffles can reach 235.56 mL/min.

Concurrent with structural design research on valveless piezoelectric pumps, researchers have also employed numerical computation methods to analyze the velocity and pressure distribution within the pump's internal flow field, as well as the pressure loss coefficients of the channels, with the aim of optimizing the structural dimensions of the piezoelectric pump and enhancing its output performance [22–24]. However, this analytical approach is incapable of pinpointing the exact locations where energy losses occur. In contrast, the entropy production method provides a means of linking unstable flow with energy losses, allowing for the precise calculation of the specific sites of energy loss. Huang et al. [25] applied the entropy production method to conduct energy loss analyses on the hyperbolic channel, and subsequently optimized the structure of the flow-resistant differential channels based on the computational outcomes. The experimental results demonstrated that the output performance of the optimized piezoelectric pumps was significantly superior to that prior to optimization. However, the study focused solely on the optimization of the flow-resistant differential channels and did not encompass the entire piezoelectric pump.

Therefore, to gain an in-depth understanding of the impact of airfoil angle of attack on the flow field structure within the channel and the output performance of piezoelectric pumps, this study positioned the Clark Y airfoil within the channel and designed valveless piezoelectric pumps with airfoil baffles at various angles of attack. Experimental studies were conducted to investigate the output performance of the valveless piezoelectric pumps with airfoil baffles at different angles of attack. Subsequently, full-flow field simulations were performed on the piezoelectric pumps, integrating the entropy production theory and the Q criterion to study the energy dissipation characteristics of various components within the pump. This investigation elucidates the influence of changes in the airfoil angle of attack on energy dissipation within the flow field of the piezoelectric pump.

2. Structural Design and Working Principle

Figure 1 illustrates the assembly schematic of a valveless piezoelectric pump with airfoil baffles. The pump primarily consists of inlet and outlet tubes with airfoil baffles (Number Name Clark Y), a pump chamber, a cover plate, and a piezoelectric vibrator with PZT-5A piezoelectric ceramic material. The pump body is assembled using a bolt connection method. In order to facilitate the smooth installation of the pipe in the pump flow and pressure test, and reduce the energy loss caused by the pipe diameter mismatch, we used a straight tube for the inlet and an elbow tube (with high diameter reduction) for the outlet. Table 1 presents the structural parameters of the piezoelectric pump.

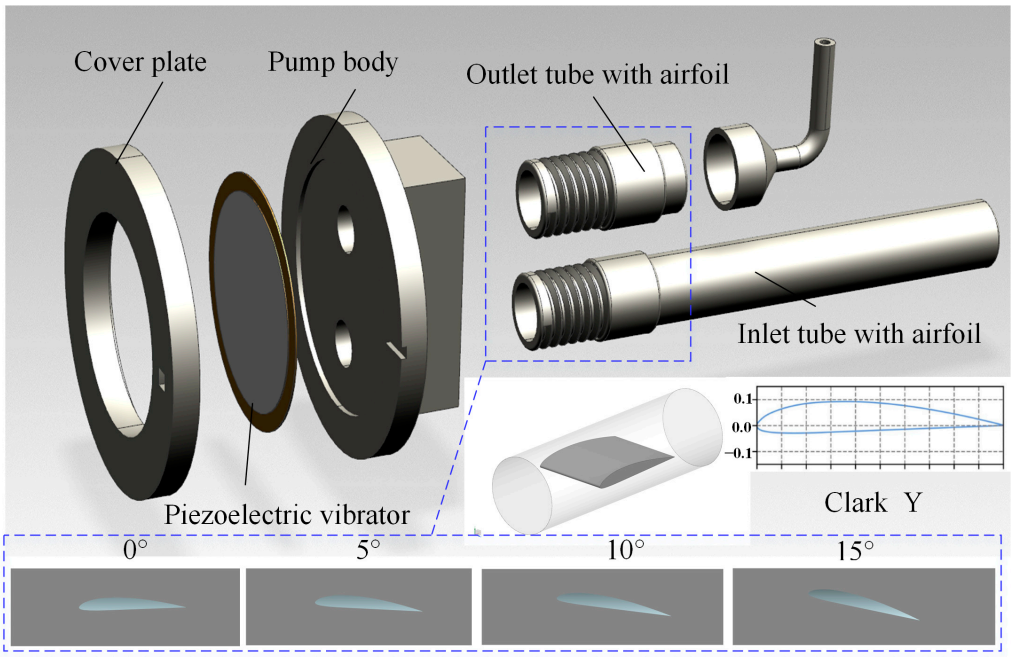


Figure 1. Assembly diagram of the valveless piezoelectric pump with airfoil baffles.

Table 1. Structural parameters.

Parameters	Value
Chamber diameter	38 mm
Chamber depth	3 mm
Vibrator diameter	40 mm
Airfoil chord length	10 mm
Tube length	27 mm
Inlet tube diameter	8 mm
Outlet elbow tube diameter	3 mm
Distance between airfoil and chamber	12.5 mm

Figure 2 depicts the working principle schematic of the valveless piezoelectric pump with airfoil baffles. The piezoelectric vibrator, excited by an alternating voltage, vibrates, causing periodic changes in the volume of the pump chamber. When the volume of the pump chamber increases, the pressure within the chamber decreases, and external fluid, under the influence of a pressure differential, flows into the pump chamber through the inlet and outlet tubes. This phase is known as the suction mode of the piezoelectric pump. Conversely, when the volume of the pump chamber decreases, the pressure within the chamber rises, and the fluid, again under the influence of a pressure differential, flows out of the pump chamber through the inlet and outlet tubes. This phase is referred to as the pumping mode of the piezoelectric pump. According to Ref. [21], the fluid encounters less resistance when flowing from the leading edge to the trailing edge of the airfoil baffle (forward flow) compared to when it flows from the trailing edge to the leading edge (reverse flow), where the resistance is greater than that of the forward flow. Due to the unequal flow resistance generated by the fluid flowing over the airfoil baffle in both directions, the flow rates into and out of the inlet and outlet tubes during the suction and pumping processes of the piezoelectric pump are unequal. The arrow width marked in the inlet and outlet tube in Figure 2 represents the flow size. Thus, with the vibration of the piezoelectric vibrator, the pump can macroscopically produce a unidirectional pulsating output.

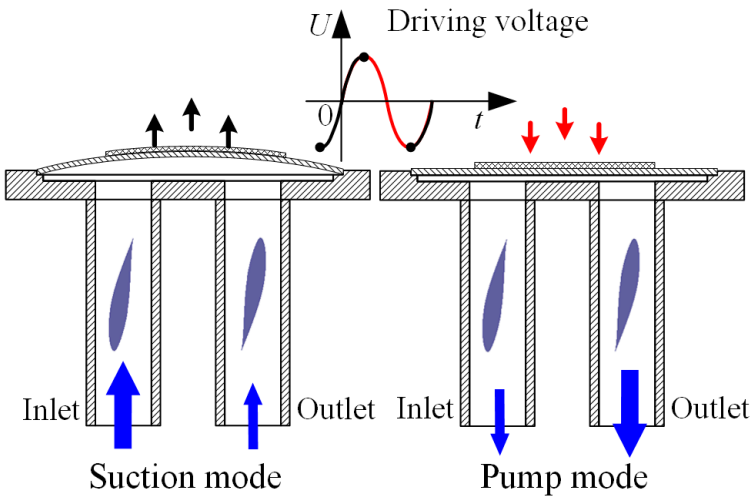


Figure 2. Schematic diagram of the working principle.

When the piezoelectric ceramic material is PZT-5A and the driving voltage is a sinusoidal function of the peak-to-peak value of 200 V, the flow resistance of the tubes significantly affects the output performance of the piezoelectric pump. The pressure loss coefficient (flow resistance coefficient) of the tube containing the airfoil baffle is denoted as follows:

$$\xi = \frac{\Delta p}{\rho v^2/2} \tag{1}$$

where Δp represents the pressure difference at the inlet and outlet of the tube with an airfoil baffle, ρ is the fluid density, and v is the average velocity of the fluid flowing through the outlet of the tube with an airfoil baffle.

According to the Ref. [11], the output flow rate of the valveless piezoelectric pump with airfoil baffles can be expressed as follows:

$$V_0 = 2\Delta V f \left(\frac{\eta^{\frac{1}{2}} - 1}{\eta^{\frac{1}{2}} + 1} \right) \tag{2}$$

$$\eta = \frac{\xi_b}{\xi_a} \tag{3}$$

Here, f is the driving frequency of the piezoelectric vibrator, ΔV is the volumetric change in the pump chamber when the vibrator moves to its highest position, η is the ratio of the forward to reverse flow resistance coefficients of the tube, also known as the impedance ratio, ξ_a is the forward flow resistance coefficient, and ξ_b is the reverse flow resistance coefficient. The greater the impedance ratio, the stronger the unidirectional cut-off ability in the tube, and the easier it is to form the macroscopic flow as shown in Figure 2. From Equation (2), it is evident that $\xi_a \neq \xi_b$, enabling the unidirectional transport of fluid by the valveless piezoelectric pump. The valveless piezoelectric pump possesses the capability for unidirectional flow, enabling the transportation of fluid in a singular direction without the necessity for unidirectional flow control valves. Furthermore, as the angle of attack of the airfoil changes, the flow resistance coefficients of the tube are affected, consequently influencing the output performance of the valveless piezoelectric pump with airfoil baffles.

3. Experimental Setup

The schematic diagram of the output performance test for the valveless piezoelectric pump with airfoil baffles is depicted in Figure 3. A signal generator (AFG 3022B, Tektronix Beaverton, OR, USA) and power amplifier (HVP-300D, NJFN, Nanjing, China) provide a driving voltage of 100 V to excite the piezoelectric vibrator. The parameters of the piezoelectric vibrators are shown in Table 2 [26]. Starting from 0° angle of attack, inlet and outlet pipes with airfoil baffles of the same angle are selected to assemble a valveless piezoelectric pump for multiple experiments. Subsequently, the driving frequency is adjusted to obtain different working frequency intervals between different experimental groups. Experiments are conducted within respective working ranges, each with a variation of 1 Hz. Utilizing an analytical balance with a precision of 0.001 g [27], the mass of liquid output by the valveless pump per unit time is measured to obtain the relationship curve between the output flow rate and driving frequency at zero back pressure for the valveless piezoelectric pump with airfoil baffles. During the flow rate test, a laser displacement sensor (LK-G35, Keyence, Osaka, Japan) is employed to measure the displacement of the center point of the circular vibrator. The test results are used to set the boundary conditions for the flow field simulation. A straight pipe is connected at the outlet of the piezoelectric pump, and the height difference in the liquid level at the inlet and outlet is recorded under different driving frequencies to obtain the relationship curve between the output back pressure at zero flow rate and the frequency for the valveless piezoelectric pump.

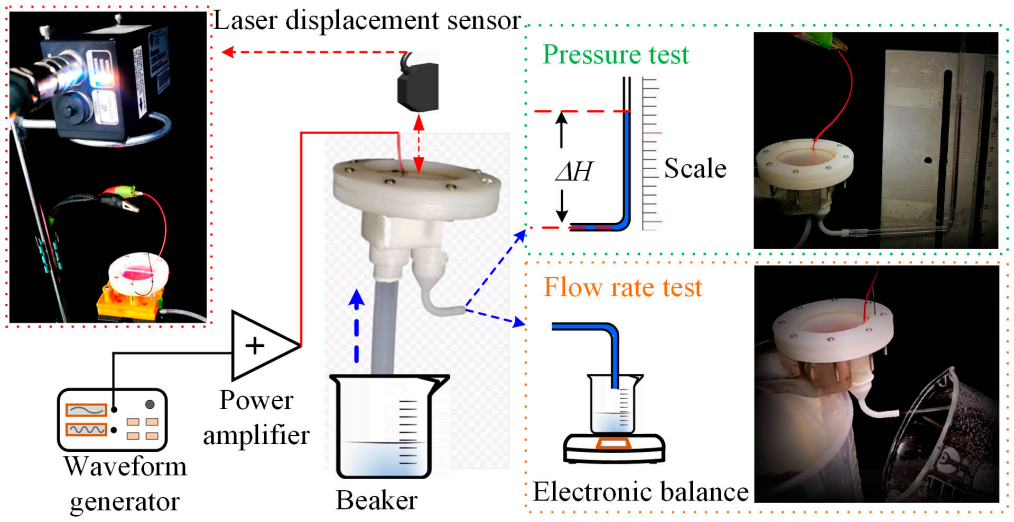


Figure 3. Experimental schematic diagram.

The types of fluids suitable for piezoelectric micropumps mainly include pure water, alcohols, ketones, and non-strong acids and bases with low viscosity values. In addition, considering electrolyte interference, experimental cleaning efficiency, environmental protection, and economy, deionized water was used as the working medium in all tests.

Table 2. Material parameters of the PZT vibrator.

Material	Young's Modulus (GPa)	Piezoelectric Constant ($C \cdot m^{-2}$)	Permittivity (F/m)	Poisson's Ratio	Density ($kg \cdot m^{-3}$)	Resonant Frequency (kHz)
Beryllium bronze	128	/	/	0.35	8600	/
PZT-5A	$\begin{bmatrix} 121 & 75.4 & 75.2 & 0 & 0 & 0 \\ 75.4 & 121 & 75.2 & 0 & 0 & 0 \\ 75.2 & 75.2 & 111 & 0 & 0 & 0 \\ 0 & 0 & 0 & 21.1 & 0 & 0 \\ 0 & 0 & 0 & 0 & 21.1 & 0 \\ 0 & 0 & 0 & 0 & 0 & 22.6 \end{bmatrix}$	$\begin{bmatrix} 0 & 0 & -5.4 \\ 0 & 0 & -5.4 \\ 0 & 0 & 15.8 \\ 0 & 12.3 & 0 \\ 12.3 & 0 & 0 \\ 0 & 0 & 0 \end{bmatrix}$	$\begin{bmatrix} 8.107 & 0 & 0 \\ 0 & 8.107 & 0 \\ 0 & 0 & 7.346 \end{bmatrix} \times 10^{-9}$	/	7750	1.3 ± 0.5

4. Flow Field Simulation

To establish different models of valveless piezoelectric pumps with airfoil baffles, four angles of attack were chosen for the Clark Y airfoil: 0°, 5°, 10°, and 15°. Continuing to increase the angle of attack of the airfoil leads to an enlargement of the diameter of the inlet and outlet tubes, thereby increasing the pump chamber diameter. Considering the dimensions of the piezoelectric vibrator used in the experiment, this study sets the maximum angle of attack of the airfoil at 15°. Simulations of the transient flow field in piezoelectric pumps were performed utilizing the CFX software, with calculations of entropy generation carried out for three distinct areas: (1) the pump chamber, (2) the airfoil baffle region, and (3) the outlet bend, as illustrated in Figure 4. The maximum displacement data obtained from a laser displacement sensor for a circular piezoelectric vibrator were configured as the motion parameter for the vibration on the upper surface of the pump chamber, with the optimal output frequency corresponding to the vibration frequency of the upper surface of the pump chamber under the given airfoil angle condition, with the inlet and outlet set to atmospheric pressure and the no-slip condition applied to the walls of the computational domain. The fluid was assumed to be incompressible, and the SIMPLE algorithm was employed to obtain the velocity and pressure coupling solution. The numerical convergence residual was 10^{-5}. The working fluid was deionized water, characterized by a density of 1000 kg/m^3, and a dynamic viscosity of 1×10^{-3} Pa·s.

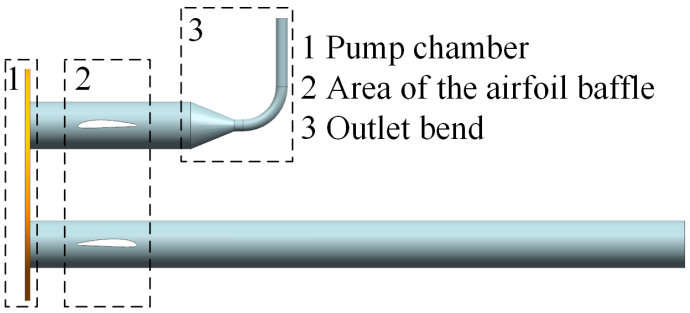


Figure 4. Flow field simulation model.

As the fluid moves through the pump, mechanical energy is transformed into internal energy due to the fluid's viscosity and Reynolds stresses, leading to entropy generation within the pump. This generation is primarily attributed to three factors: direct dissipation from the fluid's mean velocity, turbulence dissipation from the fluid's pulsation velocity, and wall dissipation due to the high velocity gradient near the pipe wall, which is the result of fluid viscosity.

The formula for the rate of entropy generation due to the mean velocity is as follows:

$$s_{D1} = \frac{\mu}{T}\left[\left(\frac{\partial \overline{u}}{\partial y}+\frac{\partial \overline{v}}{\partial x}\right)^2+\left(\frac{\partial \overline{u}}{\partial z}+\frac{\partial \overline{\Omega}}{\partial x}\right)^2+\left(\frac{\partial \overline{\mu}}{\partial y}+\frac{\partial \overline{\Omega}}{\partial y}\right)^2\right]+2\frac{\mu}{T}\left[\left(\frac{\partial \overline{u}}{\partial x}\right)^2+\left(\frac{\partial \overline{v}}{\partial y}\right)^2+\left(\frac{\partial \overline{\Omega}}{\partial z}\right)^2\right] \quad (4)$$

The rate of entropy generation due to pulsation velocity is as follows:

$$s_{D2} = \frac{\mu_{eff}}{T}\left[\left(\frac{\partial \mu'}{\partial y}+\frac{\partial v'}{\partial x}\right)^2+\left(\frac{\partial u'}{\partial z}+\frac{\partial v'}{\partial x}\right)^2+\left(\frac{\partial u'}{\partial y}+\frac{\partial \Omega'}{\partial y}\right)^2\right]+2\frac{\mu}{T}\left[\left(\frac{\partial u'}{\partial x}\right)^2+\left(\frac{\partial v'}{\partial y}\right)^2+\left(\frac{\partial \Omega'}{\partial z}\right)^2\right] \quad (5)$$

Here, $\overline{u}$, $\overline{v}$, $\overline{w}$ represent the mean velocity components in the x, y, z directions in m/s; u', v', w' are the pulsation velocity components in the same directions in m/s; T is the temperature in K; μ is the dynamic viscosity of the fluid in Pa·s; and μ_{eff} is the effective

dynamic viscosity, also in Pa·s, which can be determined using the formula (6), where μ_t is the turbulent dynamic viscosity in Pa·s.

$$\mu_{\text{eff}} = \mu + \mu_t \tag{6}$$

Since the pulsation velocity components are not calculable in the Reynolds-averaged equations, the rate of entropy generation due to pulsation velocity can be estimated using Formula (7), where the empirical coefficient β = 0.09, f is the characteristic frequency of turbulence in Hz, k is the turbulent kinetic energy in m^2/s^2, and ρ is the density in kg/cm^3.

$$s_{D2'} = \beta \frac{\rho f k}{T} \tag{7}$$

By integrating these components of the entropy production rate over the defined region, the direct dissipation entropy production $S_{\overline{D1}}{}'$ (W/k) and turbulence dissipation entropy production $S_{\overline{D2}}{}'$(W/k) can be derived.

$$S_{\overline{D1}}{}' = \int s_{D1} dV \tag{8}$$

$$S_{\overline{D2}}{}' = \int s_{D2'} dV \tag{9}$$

The formula for entropy generation near the wall is as follows:

$$S_{D3} = \int_A \frac{\vec{\tau} \cdot \vec{v}}{T} dA \tag{10}$$

where τ is the wall shear stress in Pa, A is the area in m^2, and $\vec{v}$ is the velocity near the wall surface in m/s.

Thus, the total entropy production within the computational domain is as follows:

$$S_D = S_{\overline{D1}}{}' + S_{\overline{D2}}{}' + S_{D3} \tag{11}$$

To examine the correlation between entropy generation and the flow field structure within the pump, especially when the output flow rate of the piezoelectric pump is affected by changes in the airfoil baffle's angle of attack, it is essential to determine the characteristics of the vortices within the pump. This study used the Q criterion for identifying vortices in the computational results.

The Q criterion is defined as follows:

$$Q = \frac{1}{2}\left(\Omega_{ij}\Omega_{ij} - S_{ij}S_{ij}\right) \tag{12}$$

where Ω_{ij} is the rotation tensor and S_{ij} is the strain rate tensor. A positive Q value indicates the presence of vortex structures in the flow field, with a higher Q value signifying greater vortex strength.

Considering the accuracy of the computational results and the computational time, a mesh independence study was conducted on the computational domain prior to calculations, using mesh cell numbers of 1.6 million, 1.8 million, 2 million, and 2.2 million for validation. Taking the flow simulation values of the 2.2 million mesh model as a benchmark for verification, the results of the mesh independence verification for the model are shown in Table 3. Consequently, this study selected a mesh scheme with approximately 2 million mesh cells for numerical computation.

Table 3. Results of the mesh independence verification.

No.	Mesh Number	Net Output Flow Ratio
G1	1.6 million	94.197%
G2	1.8 million	97.454%
G3	2.0 million	98.581%
G4	2.2 million	/

5. Results and Discussion

Figure 5 illustrates the experimental performance curves of the valveless piezoelectric pump with airfoil baffles at various angles of attack. Specifically, Figure 5a illustrates the relationship between flow rate and frequency for these pumps. It can be observed that the output flow rate of the pumps varies significantly with changes in the driving frequency of the piezoelectric vibrator, and this output flow rate decreases as the angle of attack of the airfoil increases. At an angle of attack of 0° for the Clark Y airfoil, the maximum output flow rate of the pump is 200.7 mL/min. At an angle of attack of 15°, the maximum output flow rate is reduced to 163.4 mL/min. Within the frequency range of 30–43 Hz, the pump with an airfoil angle of attack of 5° exhibits a higher output flow rate compared to that with an angle of attack of 0°. Figure 5b presents the back pressure–frequency curves of the piezoelectric pumps. The output back pressure of the valveless piezoelectric pumps increases and then decreases with an increase in piezoelectric vibrator driving frequency, and this maximum back pressure decreases with an increase in the airfoil angle of attack. Specifically, at an angle of attack of 0° for the Clark Y airfoil, the maximum output back pressure of the pump is 784.4 Pa, and at an angle of attack of 15°, it is reduced to 600.7 Pa. The results show that the valveless piezoelectric pump with airfoil baffles has a high output flow, so it is suitable for applications with a large flow demand. Figure 6 presents the experimental displacement values of the piezoelectric vibrator and the simulated flow rates of the pump. It can be observed that as the angle of attack of the airfoil increases, the maximum amplitude of the vibrator decreases. At an angle of attack of 0°, the central maximum amplitude of the piezoelectric vibrator reaches 53 μm. When the airfoil angle of attack is 15°, the maximum error between the simulated and experimental flow rates of the piezoelectric pump is 14%. This discrepancy arises from the use of the maximum amplitude at the center point of the piezoelectric vibrator as the displacement load in the flow field simulation, which consequently results in the simulated values being slightly higher than the experimental values.

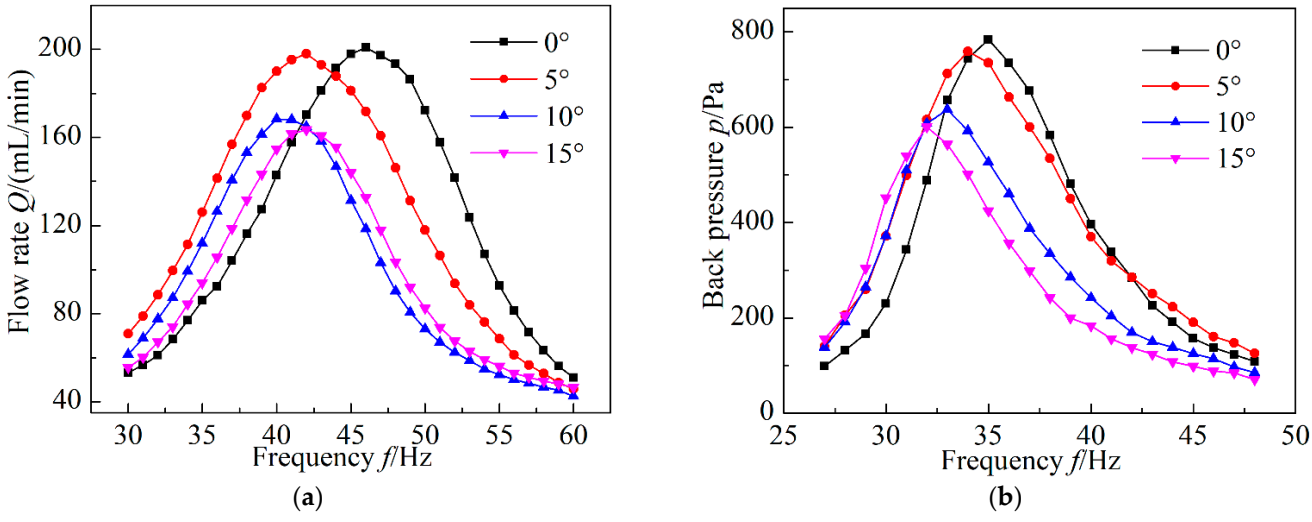


Figure 5. Performance curves of the valveless piezoelectric pump with airfoil baffles: (**a**) flow rate–frequency curve; (**b**) back pressure–frequency curve.

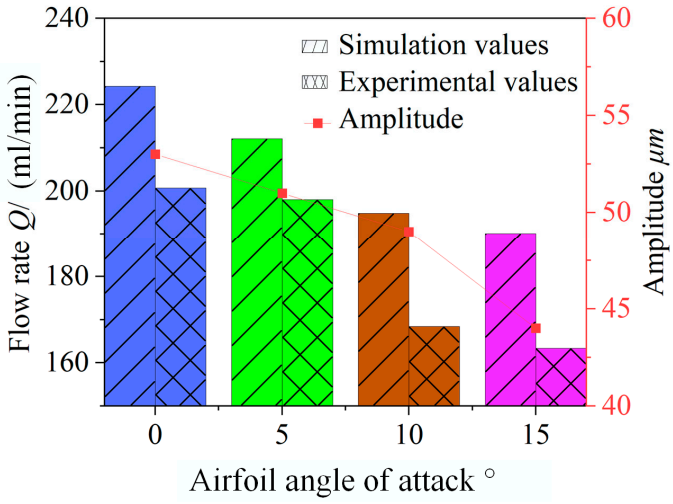


Figure 6. Displacement of vibrator and pump flow rate.

Figure 7 presents the entropy production curves of valveless piezoelectric pumps with airfoil baffles at various angles of attack. The results indicate that as the angle of attack of the airfoil increases, the entropy production within the piezoelectric pump also gradually increases, with turbulence dissipation entropy production and wall entropy production constituting a larger proportion compared to viscous entropy production.

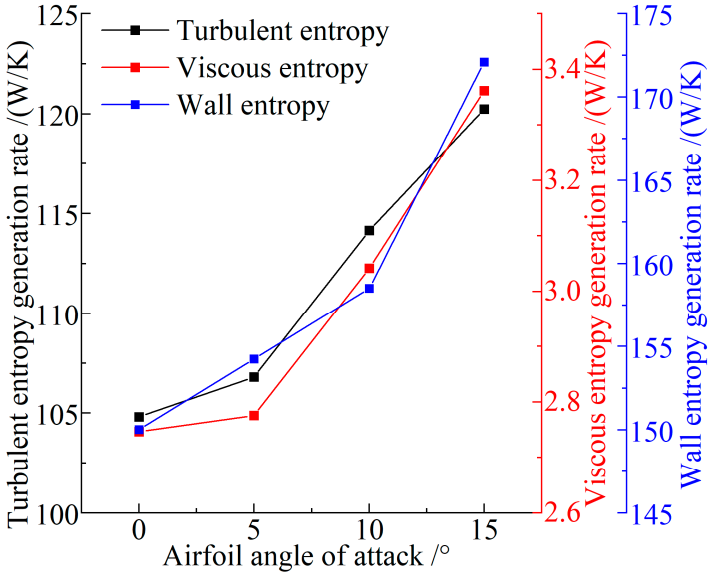


Figure 7. Entropy production curves of the pumps.

Figure 8 illustrates the turbulence entropy production contour maps and vortex structure distribution of the valveless piezoelectric pumps with airfoil baffles at different angles of attack. It can be observed that the high entropy production zones within the piezoelectric pump are primarily located at the pump chamber inlet, the trailing edge of the airfoil in the inlet pipe, the trailing edge of the airfoil in the outlet pipe, and the outlet bend. The greater the angle of attack of the airfoil baffle in the valveless piezoelectric pump, the greater the turbulence dissipation entropy production and the complexity of the vortex core structure at the pump chamber inlet, the trailing edge of the airfoil in the inlet pipe, the trailing edge of the airfoil in the outlet pipe, and the outlet bend.

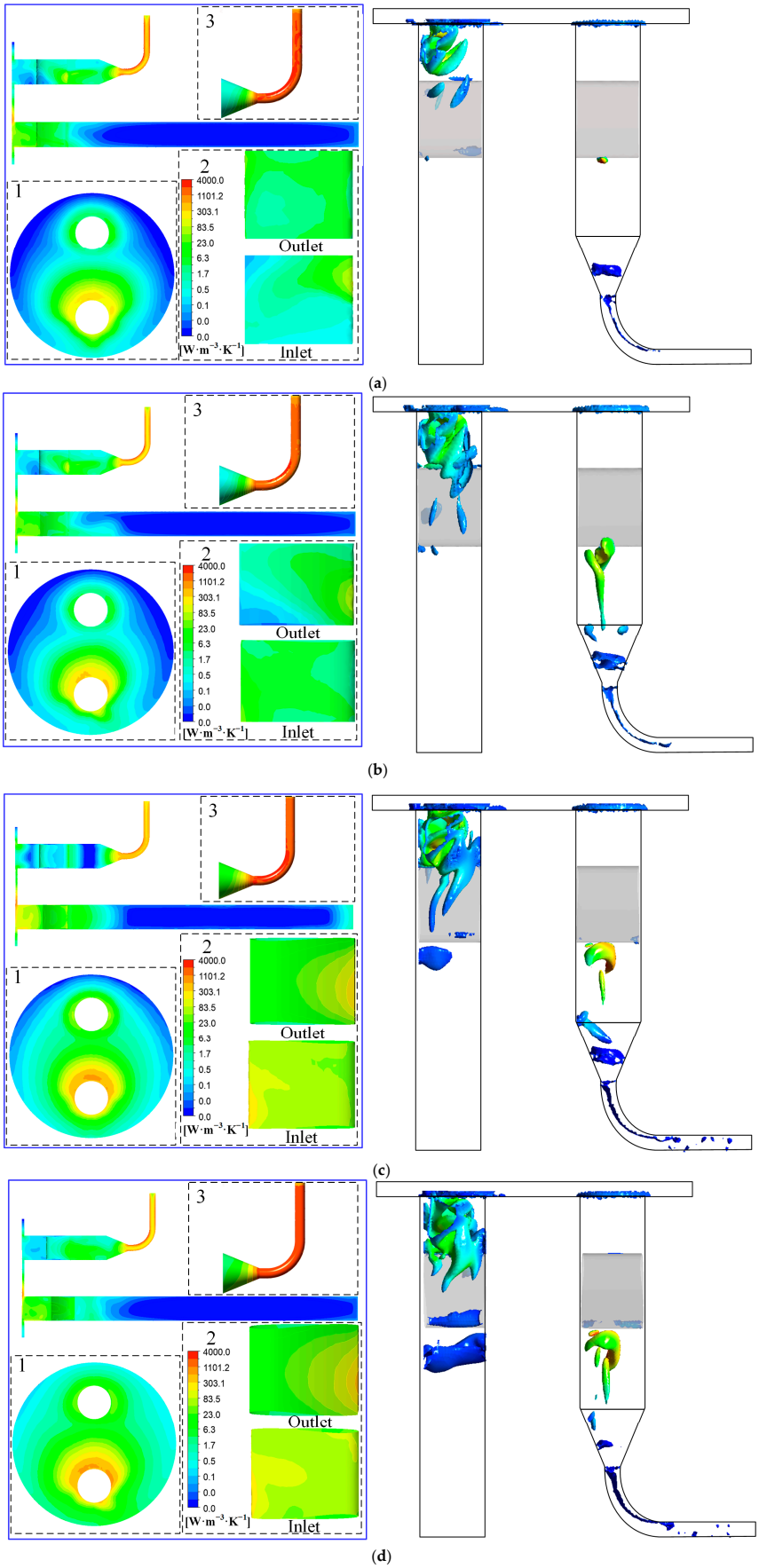


Figure 8. Turbulent entropy production (left) and vortex distribution (right) of the pump at different angles of attack: (**a**) 0°; (**b**) 5°; (**c**) 10°; and (**d**) 15°.

When the airfoil baffle is at a 0° angle of attack, the vortex core structure is relatively simple. A region of weaker vortical structures is formed between the inlet airfoil baffle and the pump chamber, while a limited yet stronger vortex core emerges between the outlet airfoil baffle and the outlet bend, subsequently converging to create a vortical structure at the outlet bend. At this moment, the fluid flow near the airfoil baffle is more stable, with less flow separation, and both the vortex and turbulence intensities are relatively low. Additionally, the low entropy production at the pump chamber inlet and outlet bend indicates minimal energy loss. When the angle of attack increases to 5°, the vortex core structure becomes more complex. The vortical structures between the inlet airfoil baffle and the pump chamber disseminate and extend towards the airfoil surface, while the vortices between the outlet airfoil baffle and the outlet bend distinctly converge. The increase in the angle of attack leads to flow separation at the trailing edge of the airfoil, forming distinct vortex cores. Concurrently, there is a significant increase in entropy production at the trailing edge of the airfoil and the outlet bend, indicating increased energy loss in these zones. At a 10° angle of attack, the vortical structures in the region between the inlet airfoil baffle and the pump chamber diffusely spread across the airfoil surface, resulting in the presence of some vortices at the leading edge of the airfoil. Although the number of vortical structures between the outlet airfoil baffle and the outlet bend does not markedly increase, the scale of these vortices is significantly enhanced. The enhancement of vortex phenomena leads to an expansion of high entropy production zones. The high entropy production zones at the trailing edge of the airfoil and the outlet bend expand significantly, resulting in a substantial increase in energy loss. This indicates that a larger angle of attack leads to increased turbulence at the leading and trailing edges of the airfoil, a more complex vortex core structure, and, consequently, increased energy loss in the flow. When the angle of attack is increased to 15°, the vortex core structure at the trailing edge of the airfoil and the outlet bend reaches its maximum complexity, and the vortex phenomena become more intense. In the area between the inlet airfoil baffle and the pump chamber, the vortices clearly diffuse, forming a complete vortical structure at the leading edge of the airfoil, while both the number and size of vortical structures between the outlet airfoil baffle and the outlet bend show significant enhancement. The larger angle of attack results in an increased area of flow separation and an expansion of vortex intensity and range, leading to significant energy loss and enhanced turbulence.

Figure 9 illustrates the proportion of wall entropy production in the total wall entropy production of different components. It can be observed that the wall entropy production is predominantly concentrated in the outlet bend component. This is attributed to the presence of a converging section and a curved section in this component, where the fluid, after passing the airfoil baffle, enters this part, leading to an increased velocity gradient. The proportion of wall entropy production for the airfoil baffle remains unchanged.

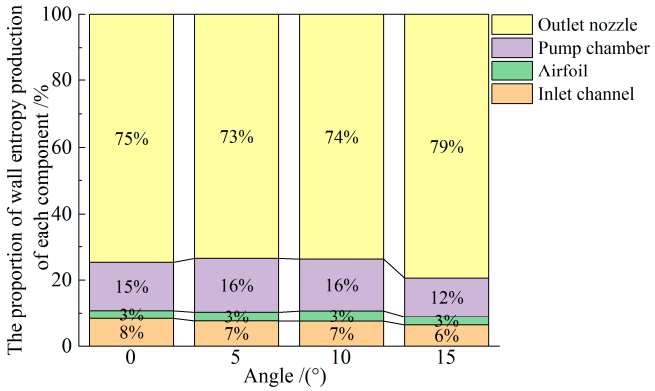


Figure 9. Proportion of wall entropy production of different components.

6. Conclusions

To deeply understand the impact of the airfoil angle of attack on the output performance of valveless piezoelectric pumps with airfoil baffles, this study experimentally investigated the output characteristics of valveless piezoelectric pumps with airfoil baffles at various angles of attack, and performed simulation calculations for the entire flow field of the piezoelectric pump. The experimental results indicate that as the airfoil angle of attack increases, both the maximum output flow rate and the maximum output back pressure of the piezoelectric pump decrease. At a 0° angle of attack for the Clark Y airfoil, the maximum output flow rate of the pump is 200.7 mL/min, with a maximum output back pressure of 784.4 Pa. The flow field simulation results show that with an increase in the airfoil angle of attack, the entropy production within the piezoelectric pump also gradually increases, with turbulence dissipation entropy production and wall entropy production constituting a larger proportion compared to viscous entropy production. Notably, regions of high turbulence dissipation entropy production within the pump are primarily located at the pump chamber inlet, the trailing edge of the airfoil in the inlet pipe, the trailing edge of the airfoil in the outlet pipe, and the outlet bend. As the angle of attack of the airfoil baffle increases, the complexity of the vortex core structure in the flow field also increases. The areas of high wall entropy production are mainly concentrated in the outlet bend component.

Author Contributions: Conceptualization, J.H. and B.Z.; methodology, J.H., H.A., M.K. and J.X.; software, H.A. and M.K.; validation, H.A., M.K., J.X. and S.Z.; formal analysis, S.Z.; investigation, J.H. and H.A.; resources, B.Z.; data curation, M.K. and J.X.; writing—original draft preparation, J.H.; writing—review and editing, B.Z.; visualization, M.K.; supervision, B.Z.; project administration, B.Z.; funding acquisition, J.H. and B.Z. All authors have read and agreed to the published version of the manuscript.

Funding: This research was funded by the National Natural Science Foundation of China, grant number 51605200.

Institutional Review Board Statement: Not applicable.

Informed Consent Statement: Not applicable.

Data Availability Statement: The raw data supporting the conclusions of this article will be made available by the authors upon request.

Conflicts of Interest: The authors declare no conflicts of interest.

References

1. Pan, Q.; Li, Y.; Diao, W.; Wang, X.; Zhang, C.; Liu, S.; Li, R. Design and investigation of a resonant piezoelectric pump with high output pressure using a displacement-amplifying vibrator. *Smart Mater. Struct.* **2022**, *31*, 065023. [CrossRef]
2. Yin, Y.; Zhou, C.; Zhao, F.; Wang, L.; Ye, Z.; Jin, J. Design and investigation on a novel piezoelectric screw pump. *Smart Mater. Struct.* **2020**, *29*, 085013. [CrossRef]
3. Zhang, Y.; Li, J.; Wang, X.; Shao, J.; Liu, S.; Pan, Q. Design and research of a valve-based piezoelectric pump with low forward resistance and high reverse shutoff. *J. Micromech. Microeng.* **2023**, *33*, 105002. [CrossRef]
4. Ma, H.K.; Chen, R.H.; Yu, N.S.; Hsu, Y.H. A miniature circular pump with a piezoelectric bimorph and a disposable chamber for biomedical applications. *Sens. Actuators A Phys.* **2016**, *251*, 108–118. [CrossRef]
5. Chen, S.; Liu, H.; Ji, J.; Kan, J.; Jiang, Y.; Zhang, Z. An indirect drug delivery device driven by piezoelectric pump. *Smart Mater. Struct.* **2020**, *29*, 075030. [CrossRef]
6. Huang, J.; Li, L.; Yang, J.; Affane, H.; Zhang, Q. Experimental study on the bionic microchannel heat sink integrated with a piezoelectric pump. *Appl. Therm. Eng.* **2024**, *240*, 122282. [CrossRef]
7. Bußmann, A.; Thalhofer, T.; Hoffmann, S.; Daum, L.; Surendran, N.; Hayden, O.; Richter, M. Microfluidic cell transport with piezoelectric micro diaphragm pumps. *Micromachines* **2021**, *12*, 1459. [CrossRef]

8. McDonald, R.C.; Hamdan, M. Compact direct methanol fuel cell: Design approach using commercial micropumps. *J. Electrochem. Energy Convers. Storage* **2019**, *16*, 011003. [CrossRef]
9. Tseng, L.Y.; Yang, A.S.; Lee, C.Y.; Cheng, C.H. Investigation of a piezoelectric valveless micropump with an integrated stainless-steel diffuser/nozzle bulge-piece design. *Smart Mater. Struct.* **2013**, *22*, 085023. [CrossRef]
10. Chen, X.; Chen, Z.; Gui, Z.; Zhang, F.; Zhang, W.; Zhou, X.; Zhang, J. A novel valve-less piezoelectric micropump generating recirculating flow. *Eng. Appl. Comput. Fluid Mech.* **2021**, *15*, 1473–1490. [CrossRef]
11. Stemme, E.; Stemme, G. A valveless diffuser/nozzle-based fluid pump. *Sens. Actuators A* **1993**, *39*, 159–167. [CrossRef]
12. Morris, C.J.; Forster, F.K. Low-order modeling of resonance for fixed-valve micropumps based on first principles. *J. Microelectromech. Syst.* **2003**, *12*, 325–334. [CrossRef]
13. Fadl, A.; Demming, S.; Zhang, Z.; Büttgenbach, S.; Krafczyk, M.; Meyer, D.M. A multifunction and bidirectional valve-less rectification micropump based on bifurcation geometry. *Microfluid. Nanofluidics* **2010**, *9*, 267–280. [CrossRef]
14. Huang, J.; Zou, L.; Tian, P.; Wang, Y.; Zhang, Q. Development of a valveless piezoelectric pump with vortex diodes. *J. Micromech. Microeng.* **2019**, *29*, 125006. [CrossRef]
15. Yu, D.; Hu, R.; Han, L.; Yang, J.; He, L. Principle and experimental study of a combined teardrop and heart-shaped channel bluffbody valveless piezoelectric pump. *Rev. Sci. Instrum.* **2024**, *95*, 065003. [CrossRef]
16. Xia, Q.; Zhang, J.; Li, H. Valve-less piezoelectric pump with unsymmetrical slope chamber bottom. *Opt. Precis. Eng.* **2006**, *14*, 641–647.
17. He, L.; Zhao, D.; Li, W.; Xu, Q.; Cheng, G. Performance analysis of valveless piezoelectric pump with dome composite structures. *Rev. Sci. Instrum.* **2019**, *90*, 065002. [CrossRef]
18. Sheen, H.J.; Hsu, C.J.; Wu, T.H.; Chu, H.C.; Chang, C.C.; Lei, U. Experimental study of flow characteristics and mixing performance in a PZT self-pumping micromixer. *Sens. Actuators A Phys.* **2007**, *139*, 237–244. [CrossRef]
19. Li, S.; Zhao, W.; Ji, J.; Hu, C.; Hu, X. Analysis of flow resistance property for valve-less piezoelectric pump with hemisphere-segment bluff-body. *Int. J. Precis. Agric. Aviat.* **2021**, *4*, 14–21. [CrossRef]
20. Hu, D.B.; He, L.P.; Zhang, Z.; Liu, Y.M.; Cui, L.N.; Cheng, G.M. Research on a valveless piezoelectric pump with inner concave triangle structure. *Microsyst. Technol.* **2022**, *28*, 1935–1945. [CrossRef]
21. Wang, L.; Yang, J.; Affane, H.; Zhang, Q.; Huang, J.; Zhang, J. A high flow-rate single-chamber valveless piezoelectric pump with airfoil baffles. *Sens. Actuators A Phys.* **2023**, *354*, 114229. [CrossRef]
22. Singh, S.; Kumar, N.; George, D.; Sen, A.K. Analytical modeling, simulations and experimental studies of a PZT actuated planar valveless PDMS micropump. *Sens. Actuators A Phys.* **2015**, *225*, 81–94. [CrossRef]
23. Bian, K.; Huang, Z.; Bao, Q.B.; Zhang, J.; Lai, L.; Chen, X.; Chen, Z. Design and Experiment of Streamlined Piezoelectric Pump with Low Vortex and Large Flow Rate. *Trans. Nanjing Univ. Aeronaut. Astronaut.* **2020**, *37*, 155–163.
24. He, X.; Zhu, J.; Zhang, X.; Xu, L.; Yang, S. The analysis of internal transient flow and the performance of valveless piezoelectric micropumps with planar diffuser/nozzles elements. *Microsyst. Technol.* **2017**, *23*, 23–37. [CrossRef]
25. Huang, J.; Gong, J.; Wang, L.; Affane, H.; Zhang, Q.; Zhang, J. Optimal design of fluidic diode for valveless piezoelectric pump based on entropy production theory. *Sens. Actuators A Phys.* **2023**, *356*, 114342. [CrossRef]
26. Kailitech, KD-41B-13TE. Available online: https://www.kailitech.com/product/62.html (accessed on 25 December 2024).
27. Mettler Toledo, XPR5003S/AC. Available online: https://www.mt.com/cn/zh/home/products/Laboratory_Weighing_Solutions/precision-balances/XPR5003S-AC.html (accessed on 25 December 2024).

Disclaimer/Publisher's Note: The statements, opinions and data contained in all publications are solely those of the individual author(s) and contributor(s) and not of MDPI and/or the editor(s). MDPI and/or the editor(s) disclaim responsibility for any injury to people or property resulting from any ideas, methods, instructions or products referred to in the content.